*Remote Sens.* **2014**, *6*, 2213-2238; doi:10.3390/rs6032213

OPEN ACCESS

*remote sensing*

**ISSN 2072-4292**

www.mdpi.com/journal/remotesensing

*Article*

# A Synergetic Algorithm for Mid-Morning Land Surface Soil and Vegetation Temperatures Estimation Using MSG-SEVIRI Products and TERRA-MODIS Products

**Wei Zhao [1,2], Ainong Li [1,*], Jinhu Bian [1], Huaan Jin [1] and Zhengjian Zhang [1]**

[1] Institute of Mountain Hazards and Environment, Chinese Academy of Sciences, Chengdu 610041, China; E-Mails: zhaow@imde.ac.cn (W.Z.); bianjinhu@imde.ac.cn (J.B.); jinhuaan@imde.ac.cn (H.J.); zhangzj@imde.ac.cn (Z.Z.)

[2] State Key Laboratory of Resources and Environment Information System, Institute of Geographic Sciences and Natural Resources Research, Chinese Academy of Sciences, Beijing 100101, China

***** Author to whom correspondence should be addressed; E-Mail: ainongli@imde.ac.cn; Tel.: +86-28-8522-4131.

*Received: 19 December 2013; in revised form: 21 February 2014 / Accepted: 27 February 2014 / Published: 10 March 2014*

---

**Abstract:** Land surface is normally considered as a mixture of soil and vegetation. Many applications, such as drought monitoring and crop-yield estimation, benefit from accurate retrieval of both soil and vegetation temperatures through satellite observation. A preliminary study has been conducted in this study on the estimation of land surface soil and vegetation component temperature using the geostationary satellite data acquired by Spinning Enhanced Visible and Infrared Imager (SEVIRI) onboard the Meteosat Second Generation (MSG) and TERRA-MODIS data. A synergetic algorithm is proposed to derive soil and vegetation temperatures by using the temporal and spatial information in SEVIRI and MODIS products. The approach is applied to both simulation data and satellite data. For simulation data, the component temperatures are well estimated with root mean squared error (RMSE) close to 0 K. For satellite data application, reasonable spatial distributions of the soil and vegetation temperatures are derived for eight cloud-free days in the Iberian Peninsula from June to August 2009. An evaluation is performed for the estimated vegetation temperature against the near surface air temperature. The correlation analysis between two datasets is found that the R-squareds are from 0.074 to 0.423 and RMSEs are within 4 K. Considering the impact of fraction of vegetation cover (FVC) on the validation, the pixels with FVC less than 30% are excluded in the total data comparison, and an obvious improvement is achieved with R-squared from 0.231 to 0.417

and RMSE from 2.9 K to 2.58 K. The validation indicates that the proposed algorithm is able to provide reasonable estimations of soil and vegetation temperatures. It is a potential way to map soil and vegetation temperature for large areas.

**Keywords:** MODIS; SEVIRI; component temperature

## 1. Introduction

Land surface temperature (LST) is one of the most important parameters in all surface-atmosphere interactions and the energy fluxes between the atmosphere and the ground [1]. It is a key parameter in a variety of scientific studies including climatology, hydrology, ecology, biogeology, *etc*. [2–5]. Remote sensing techniques are a unique way for deriving the contiguous surface temperature on regional or global scale, and two spectral regions, which are referred to as thermal infrared (TIR, 3–15 μm) and microwave (1 mm–1 m), are commonly used to retrieve regional LST [6]. Compared with microwave, thermal infrared remote sensing exhibits the characteristics of better spatial resolution, more accurate temperature estimation, and multi-satellite sensor availability. Therefore, TIR remote sensing becomes the major way to estimate LST, and many LST estimation methods have been successfully developed with a high accuracy for different satellite sensors [6–13]. However, pixels observed by TIR remote sensing are usually mixed with various land cover types, and pure pixels rarely exist, especially for geostationary satellite data, such as those acquired by the Meteosat Second Generation (MSG) Spinning Enhanced Visible and Infrared Imager (SEVIRI) with a spatial resolution more than 3 km. Consequently, the estimated pixel LST represents the integrated effect of the whole "ensemble" (or the average temperature information) within the pixel. Although many studies attach importance to the pixel LST [14–20] or try to downscale pixel LST to conduct subpixel study [21,22], the component temperatures within the mixed pixel seem more meaningful and useful [23,24]. Notably for soil and vegetation, they are two major components of land surface. The large difference in thermal capacity between soil and vegetation induce the large difference of temperature change pattern. Soils are able to retain a larger part of the energy absorbed from the sun, whereas the low thermal capacity of leaves normally prevent their temperature to vary by more than a couple of degrees from the surrounding air temperature [25]. Therefore, the surface temperature will show different characteristics under different vegetation cover conditions. With the estimation of soil and vegetation temperatures, we can better understand the surface energy fluxes and surface soil moisture condition, which enhance the ability of drought monitor, yield estimation, and so on.

However, in remote sensing inversion, the problems are typically ill-posed as there is not enough data to result unique solutions [26] and the soil and vegetation component temperature estimation also faces this problem. To solve it, many scientists have done considerable work to increase the number of the equations by adding additional information based on some assumptions [24,27–30]. Generally, for a homogeneous isothermal surface, the directional signature of land surface thermal-infrared radiation is mainly attributed to the directional effect of the surface emissivity (LSE). However, remote sensing pixel often consists of multiple components and is a non-isothermal surface. Due to the directional effect of the component emissivities, the different illumination-observation geometries and the impact

of the pixel 3D structure on radiation emission, the pixel temperature observed by TIR sensor usually shows significant directional effect [31–36]. Furthermore, the effect is also partly induced by the temperature differences among the components and the environmental radiation.

Based on the thermal directional effect, Kimes [33] first tried to test the radiometric temperature observation at different view angles for a cotton row crop and found the sensor response differentials as great as 16.2 ℃ when going from a zenith view angle of 0 degree to one of 80 degree normal to the row direction. Wang *et al.* [37] made use of the directional information embedded in the visible and near infrared bands to invert the 3D structure parameters of the pixel, and, then, used the structure parameters in the TIR models to invert the component temperatures. Li *et al.* [27] systematically analyzed the directional effect of the observed brightness temperature using ERS-2 along Track Scanning Radiometer (ATSR-2) multi-direction observation data, separated the vegetation and soil temperatures well, and further suggested that an appropriate description of the pixel was needed for the component temperature estimation. Adopting the dual-view angle measurements made by ATSR-2, Jia *et al.* [38] also proposed a practical algorithm to derive component temperatures of soil and foliage employing multi-spectral remote sensing data. In addition, a thermal model-based algorithm was developed by Shi [24] for estimating the soil and leaf temperatures over mixed pixels based on the simulated the directional radiation, and it was successfully validated by the simulation data and the field experiment data.

Obviously, most of the soil and vegetation component temperature estimation methods are based on the directional effect of the surface radiation. However, most satellite sensors normally cannot provide simultaneous acquisitions at different angles, which impede the application of the multi-angle retrieval algorithm in estimating the soil and vegetation component temperatures. Therefore, a practical method is urgently needed to derive component temperatures based on the satellite data with simultaneous observation at single one view direction. To facilitate the estimation of component temperatures, additional information is required when the multi-angle information cannot be provided. The rich temporal information within the geostationary satellite data offers a good opportunity. In this study, on the basis of MSG-SEVIRI products and TERRA-MODIS products, we developed a synergetic algorithm by using the rich temporal information of SEVIRI products combined with the spatial information from MODIS products to derive the soil and vegetation component temperatures during the mid-morning period. The performance of the algorithm was evaluated by the simulation data and satellite data acquired in the Iberian Peninsula respectively.

## 2. Methodology

As we cannot directly derive the component temperature from satellite data, additional assumptions are required. Many scientists have done much work to increase the number of the equations by adding additional information based on some assumptions to solve this problem [24,27,28,38]. The multi-angle algorithms proposed by [27,38,39] are developed under the assumption that the pixel is composed of soil and vegetation, and its thermal directional effect is induced by the vegetation cover differences under different view angles. However, for single view angle satellite data, the vegetation cover is constant. Therefore, some other information like the spatial or temporal information should be utilized to increase the number of equations and complete the component temperature estimation.

Generally, on the basis of the radiative transfer theory, the radiance $B_\lambda$ measured from the sensor at the top of atmosphere (TOA) in channel $\lambda$ under a zenith observation angle $\theta$ is given by:

$$B_\lambda(T_\lambda,\theta)=\varepsilon_{\lambda,\theta}B_\lambda(T_{sur},\theta)\tau_{\lambda,\theta}+R^{\uparrow}_{atm,\lambda,\theta}+(1-\varepsilon_{\lambda,\theta})R^{\downarrow}_{atm,\lambda}\tau_{\lambda,\theta} \quad (1)$$

It includes three parts: the surface emission that is attenuated by the atmosphere, the upwelling atmosphere emission towards the sensor, and the downwelling atmosphere emission that is reflected in the surface and reaches the sensor. In the equation, $B_\lambda$ is the Planck function, $B_\lambda(T_{sur},\theta)$ is the radiance measured if the surface was a black body with surface temperature $T_{sur}$, $R^{\uparrow}_{atm,\lambda,\theta}$ is the atmospheric upwelling radiance at zenith angle $\theta$, $\varepsilon_{\lambda,\theta}$ is the surface channel emissivity at zenith angle $\theta$, $\tau_{\lambda,\theta}$ is the total atmospheric path transmittance at zenith angle $\theta$, and $R^{\downarrow}_{atm,\lambda}$ is the channel downwelling atmospheric radiance from the whole hemisphere in channel $\lambda$.

After neglecting the atmospheric effect, we can get the directional radiance ($L_{sur}$) emitted by the surface itself. Usually, except for water surfaces and impervious surfaces, most land surfaces can be regarded as a mixture of soil and vegetation. Therefore, the radiance $L_{sur}$ can be expressed by the linear integration of the radiances emitted by the soil surface and vegetation surface within the observed pixel [27,39]:

$$L_{sur}=\varepsilon(\theta)B(T_{sur})=a_v(\theta)\varepsilon_v(\theta)B(T_v)+a_s(\theta)\varepsilon_s(\theta)B(T_s) \quad (2)$$

where $a_v(\theta)$ and $a_s(\theta)$ are the area ratios of vegetation and soil in the pixel in view direction $\theta$. $a_v(\theta)$ can be also defined as the fraction vegetation cover (*FVC*) and it equals to $1 - a_s(\theta)$. $\varepsilon_v(\theta)$, $T_v$, $\varepsilon_s(\theta)$, and $T_s$ are the emissivities and temperatures of the two components respectively. $B(T_{sur})$, $B(T_v)$, and $B(T_s)$ are the thermal radiations of brightness temperature $T_{sur}$, $T_v$, and $T_s$. As we are just concerned with satellite data with only one view direction in this study, the view angle $\theta$ in the above expression is ignored in the following text.

Based on Equation (2), for each surface temperature $T_{sur}$ estimated from sensor measurement at time t for one pixel, the pixel radiometric surface temperature $T_{rad}$ can be concluded as the following expression (Equation (3)) of soil temperature $T_s$ and vegetation temperature $T_v$ without the consideration of the multiple scattering between soil and vegetation at the same time based on the study of [40] according to the Stefan-Boltzmann law. The simple linear mixture model is also approved by Menenti *et al.* [39]. According to the research in [41], usually $n \approx 4$ is reasonable for 8–14 and 10–12 μm wavelength bands. Therefore, the n value in Equation (3) is set to 4 in this study. It is clear that the soil temperature and vegetation temperature cannot be directly derived by Equation (3) alone. Under the condition that the variables *FVC*, $\varepsilon_v$, $\varepsilon_s$, and $T_{rad}(t)$ are provided in the equation at time *t*, the number of the unknowns ($T_v(t)$ and $T_s(t)$) is greater than the equation number. Therefore, the right values of $T_v(t)$ and $T_s(t)$ are unsolvable.

$$T_{rad}(t)=\varepsilon^{1/4}T_{sur}(t)=\left[FVC\varepsilon_v T_v(t)^n+(1-FVC)\varepsilon_s T_s(t)^n\right]^{1/n} \quad (3)$$

As reported by the studies of [17,42,43], the LST mid-morning rising approximates to a linear rising process when the sky is clear, thus the pixel radiometric temperature is expressed as the following equation:

$$T_{\mathrm{rad}}(t)=a_{rad}t+b_{rad} \quad (4)$$

where $a_{rad}$ is the temperature rising rate (K/h), $b_{rad}$ is the intercept (K) and t is time (h). The time period is usually from 8 a.m. to 11 a.m. (local time). It is assumed that the same phenomenon is likely to happen to soil and vegetation components. The soil temperature and vegetation temperature temporal variation is written as:

$$\begin{cases} T_v(t) = a_v t + b_v \\ T_s(t) = a_s t + b_s \end{cases} \tag{5}$$

where $a_v$ and $a_s$ are the rising rates of vegetation and soil temperature, while $b_v$ and $b_s$ are the intercepts.

In light of Equations (3) and (5), the pixel radiometric temperature is rewritten as:

$$T_{rad}(t) = \left[ FVC\varepsilon_v (a_v t + b_v)^4 + (1 - FVC)\varepsilon_s (a_s t + b_s)^4 \right]^{1/4} \tag{6}$$

Equation (6) shows that the pixel radiometric temperatures during the mid-morning period are determined by the rising rates and intercepts of both soil and vegetation temperatures. Taking n pixel temperatures observed in this period as an example, the unknowns are significantly reduced from 2n (n soil temperatures and n vegetation temperatures) to only 4 ($a_v$, $b_v$, $a_s$, and $b_s$). With the approximation, it is possible to derive the soil and vegetation temperatures during the mid-morning period.

However, because the pixel temperature mid-morning variation is also a linear rising process, great uncertainty, arising from the high correlation, will occur in the estimation of the component temperatures with a single pixel observation. In this case, it will be an optimal way to introduce the neighboring pixel observations with different *FVCs* into the calculation. Under this condition, the component temperatures of the neighboring pixels are assumed to be consistent with those of the center pixel. The number of the neighboring pixels is determined by the differences between their *FVC* and the center one within a moving window.

Grounded on the approximations and assumptions provided above, the estimation of the component temperatures is simplified to minimize the cost function shown as below.

$$C(a_v, b_v, a_s, b_s) = \min \left\{ \frac{1}{pq} \sum_{i=1}^{p} \sum_{j=1}^{q} w_i \left( \left[ \begin{array}{l} FVC_i \varepsilon_v (a_v t_j + b_v)^4 \\ + (1 - FVC_i)\varepsilon_s (a_s t_j + b_s)^4 \end{array} \right]^{1/4} - T_{rad_{i,j}}(t) \right)^2 \right\} \tag{7}$$

where $p$ is the number of the pixels in the moving window, $q$ is the number of the pixel temperature observations during the mid-morning period, and $w_i$ is the weight which is controlled by the distance to the center pixel. In this study, it is assumed that the closer pixel has greater weight than the farther one. Therefore, the weight of the center pixel was set to 0.5, and the neighboring pixels shared the rest 0.5. Figure 1 shows an example of a 5 by 5 window as an example. The center pixel has the highest weight and the others decrease with the increase of the distance to the center pixel.

**Figure 1.** Weight distribution in a 5 by 5 window.

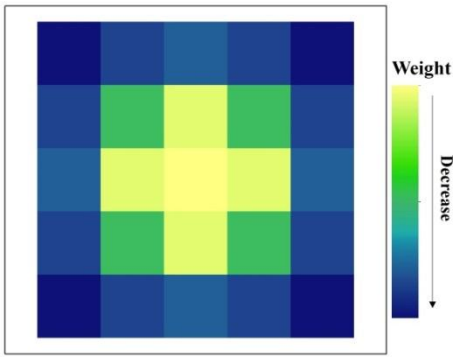


During the computation process, some additional conditions were added to constrain the estimated vegetation and soil temperatures, enabling them to display reasonable values. These conditions are:

(1) Vegetation temperature is always lower than soil temperature;
(2) Vegetation temperature is lower than pixel temperature;
(3) Soil temperature is higher than pixel temperature;
(4) The rising rate of vegetation temperature is lower than those of soil temperature and pixel temperature;
(5) The rising rate of soil temperature is higher than that of pixel temperature;
(6) Vegetation temperature is higher than the minimum temperature of the pixel from mid-night to early morning;
(7) The soil and vegetation temperature should be no more than the soil and vegetation temperature estimated from MODIS products at the TERRA overpass time in the daytime.

For the seventh condition, it is an additional limitation added in the component temperature estimation process. Considering the difference in spatial resolution for SEVIRI products and MODIS products, it can be assumed that the MODIS pixels in one SEVIRI pixel have the same soil and vegetation temperature. Therefore, soil and vegetation temperature can be estimated using these MODIS pixels to represent the values of the corresponding SEVIRI pixel, and the rule is set that the soil and vegetation temperature in the estimation should be no more than the vegetation and soil temperature estimated from MODIS products at the TERRA overpass time in the daytime.

For soil and vegetation temperature estimation using MODIS products, it was based on the temperature-vegetation index method (TVX) [15,44]. The impacts of vegetation cover differences on the average surface thermal characteristics and the evaporative control of energy partitioning induce the strong and negative correlation between vegetation index and LST. Therefore, the soil and vegetation temperature can be retrieved using the negative relationship at the corresponding NDVI values representing bare soil and full vegetated surface as shown in Equation (8).

$$\begin{cases} T_s = k * NDVI_{min} + b \\ T_v = k * NDVI_{max} + b \end{cases} \quad (8)$$

where $k$ and $b$ are the slope and intercept of the linear regression between $NDVI$ and LST.

According to the study of Prihodko and Goward [45], the $NDVI_{min}$ and $NDVI_{max}$ were assigned to 0.2 and 0.86 respectively. With the derived soil and vegetation temperature from MODIS data, the

estimated soil and vegetation temperatures should satisfy that their values are equal to or lower than the estimated soil and vegetation temperatures from MODIS products.

## 3. Data Preparation

### *3.1. Satellite Data*

The MSG-SEVIRI products was selected due to its high temporal resolution (15 min) compared with polar orbiters, e.g., NOAA AVHRR, MODIS. The MSG satellite is a kind of new generation geostationary satellite whose main payload SEVIRI includes 12 separate channels in the visible/near infrared and infrared region. The repeat cycle for its earth imaging is 15 min. The spatial resolution is also greatly improved with 3 km at the sub-satellite point for standard channels, and down to 1 km for the High Resolution Visible (HRV) channel. Equipped with such good characteristics, the SEVIRI data is able to monitor weather systems throughout the diurnal cycle, with unprecedented temporal and spatial resolution, and has the unique capabilities for cloud imaging and tracking, fog detection, measurement of the Earth-surface, and cloud-top temperatures, as well as many other improved measurements [15,46–48]. Several numerical methods [49–52] have been developed to estimate land surface temperature using SEVIRI data.

In this study, the Iberian Peninsula was chosen as the study area due to its cloud-free weather compared with other part of Europe. The SEVIRI LST, LSE, and FVC products from June to August 2009, were downloaded from Land Surface Analysis Satellite Applications Facility [53] to estimate the component temperatures. These products have a sub-nadir spatial resolution of 3 km that deteriorates towards the poles, reducing to an average of 5 km at E-W direction and 3 km at N-S direction for the study area. The algorithm about LST, LSE, and FVC estimation can be referred to Wan and Dozier [54] and Garcia-Haro *et al.* [55], respectively. The retrieval of LST is based on clear-sky measurements from MSG system in the thermal infrared window (MSG-SEVIRI channels IR10.8 and IR12.0). The website provides the Product User Manual and Algorithm Theoretical Basis Document of these products. The TERRA-MODIS LST and NDVI products (MOD11A1 and MOD13A2) were also downloaded for the same period in the study area to get soil and vegetation temperature at the satellite overpass time in the daytime from the website [56] Figure 2 shows the vegetation cover of the study area on 1 July 2009. The distribution shows that a large part of the peninsula has low vegetation cover, and only the area in the north is densely covered with vegetation.

To simplify the component temperature estimation in this study, the emissivities of soil and vegetation are simply set to constant values like the study of Li *et al.* [27]. According to the LSE and FVC product downloaded from the website, linear regression result is performed between them in the study area on 1 July 2009 (Figure 3). In Figure 3, although there are some points (LSE < 0.94) deviating from the assembling points (LSE > 0.95), their amount is considerably small compared with that of the latter. Therefore, good agreement is found between two datasets, and the coefficient of the determination (R-square) is 0.912. Similar regression results can be derived for other days. Therefore, the emissivity values at FVC = 0 and FVC = 1 are set to the right values of vegetation and soil emissivities in this study. Their values are taken as $\varepsilon_v = 0.995$ and $\varepsilon_s = 0.963$, and close to those of Li *et al.* [27].

**Figure 2.** Fraction of vegetation cover (FVC) of the study area on 1 July 2009, and the locations of the meteorological stations (red points).

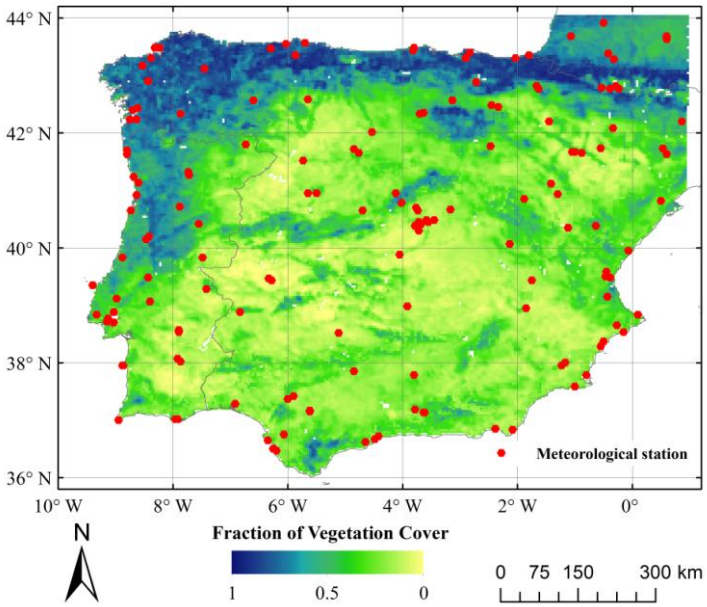


**Figure 3.** Scatter plot between fraction of vegetation cover (FVC) and emissivity in the study area on 1 July 2009.

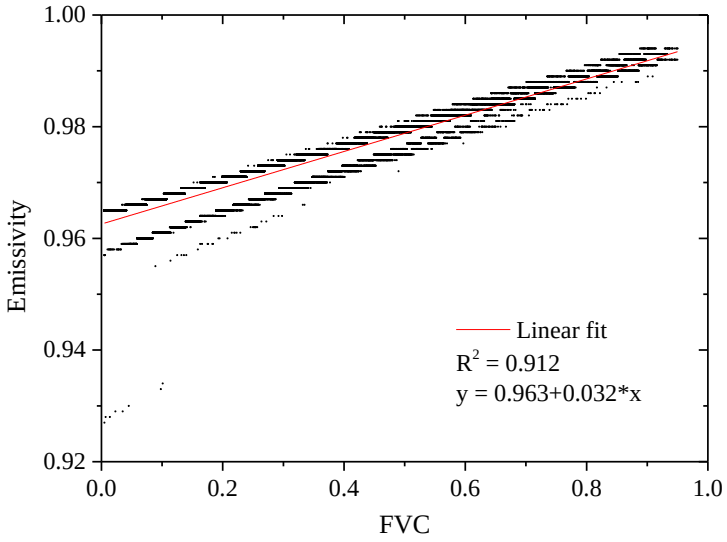


*3.2. Simulation Data*

In addition to satellite data, simulated images were also generated to validate the proposed method. Before simulation, several parameters about the component temperature information should be provided first.

In cloud-free days, it is reasonable that after the early morning dew evaporation process, soil surface temperature is usually higher than vegetation temperature during the mid-morning period with the same environmental condition (air temperature, global radiation, wind speed, *etc.*), and, thus, the rising rate of soil temperature is usually higher than that of vegetation temperature. The phenomenon

can be observed from the scatter plot between LST mid-morning rising rate and FVC in the study area on 1 July 2009 (see Figure 4a). The points distributed around the fitted line, and they are a little dispersed due to the differences of their environmental conditions. However, the negative correlation between rising rate and FVC approves the fact above. Two points (P1 and P2) approximated to bare soil surface (FVC = 0.011) and fully vegetation covered surface (FVC = 0.931) are picked out from Figure 4a. The LST mid-morning rising processes of the two points are presented in Figure 4b. It is obvious that the rising processes of the two points are well linear fitted with the coefficients of determination (R-squared) of 0.979 and 0.958, respectively. The rising rate of P1 is 6.57 K/h, and that of P2 is 1.81 K/h. The sampling points show the obvious differences of LST change under different vegetation cover conditions.

**Figure 4.** (**a**) Scatter plot between land surface temperature (LST) mid-morning rising rate and fraction of vegetation cover (FVC) in the study area on 1 July 2009. (**b**) The LST mid-morning rising processes of the two points approximating to full vegetation and bare soil.

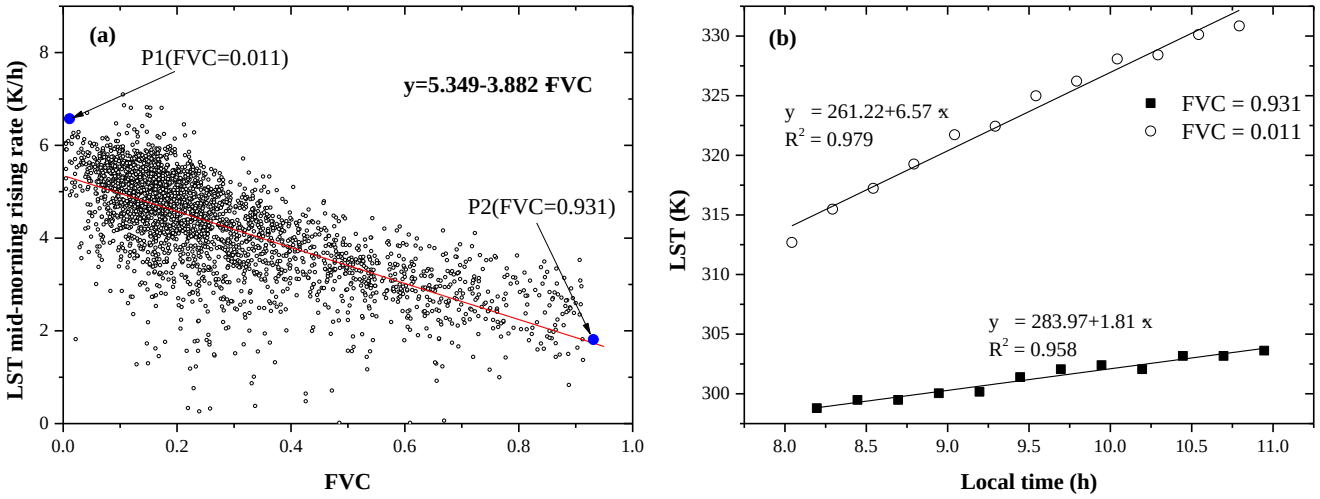


With the temperature rising information provided above, it is assumed that the mid-morning rising processes of vegetation and soil component temperature in the simulated images are similar as those of the two sampling points (P1 and P2). The rising rates of soil and vegetation temperature are set to 6.57 K/h and 1.81 K/h, and the intercepts are set to 261.22 K and 283.97 K, respectively. The time period is from 8 a.m. to 11 a.m. with a frequency of 15 min.

According to the assumed soil and vegetation temperature in the period, the simulated mixed pixel radiometric temperature can be calculated according to the Equation (6) with pre-defined FVC value and soil/vegetation emissivity. In the simulated images, it is supposed that there are only two pixels composed by soil and vegetation components and the percent of vegetation cover is determined by FVC. The two pixels have the same soil and vegetation temperature variation characteristics as shown in Figure 4b, and the radiometric temperature differences between them are majorly controlled by the FVC differences of them based on Equation (3). To validate the performance of the proposed method at different vegetation cover conditions, we simulated the mid-morning temperature rising processes of the two pixels with different vegetation cover combinations. Technically, the FVC of each pixel changed from 0 to 1 with the step of 0.02. Therefore, there are 2601 (51 × 51) cases with different FVC combinations, and they are used to evaluate the proposed method.

### *3.3. Validation Data*

As Ehrler [57] has found through experiments that leaves of most crops were essentially close to the air temperature, and the canopy-air temperature equality hypothesis is assumed valid due to heterogeneity and shade effects at the satellite pixel scale [58], the estimated component temperatures are roughly validated by comparing the derived vegetation temperature with the air temperature. Several Fixed-Weather-Stations located in the study area were selected as the reference sites (see Figure 2). The hourly air temperature data were downloaded from the NCDC climate data online system [59] from June to August 2009, and the air temperature is measured at a height of about 2 m above ground according the standard weather station regulation. As shown in Figure 2, the stations are distributed over the whole study area, and their located pixels, have quite different surface conditions (from high to low vegetation cover).

## 4. Results and Analysis

### *4.1. Application to the Simulation Data*

To evaluate the performance of the proposed method, the algorithm was firstly applied to the simulated dataset. As introduced in Section 3.2, the simulated images have two pixels. Different FVC combination of these two pixels corresponds to one case, and there are total 2601 cases. The method was run for each case to derive the component temperatures in the mid-morning period, and the estimated soil and vegetation temperatures in the period were compared with the pre-defined soil and vegetation temperatures, as shown in Figure 4b. The root mean squared error (RMSE) was derived for each case (see Figure 5).

**Figure 5.** RMSEs of soil and vegetation temperature estimation results for different fraction of vegetation cover (FVC) combinations.

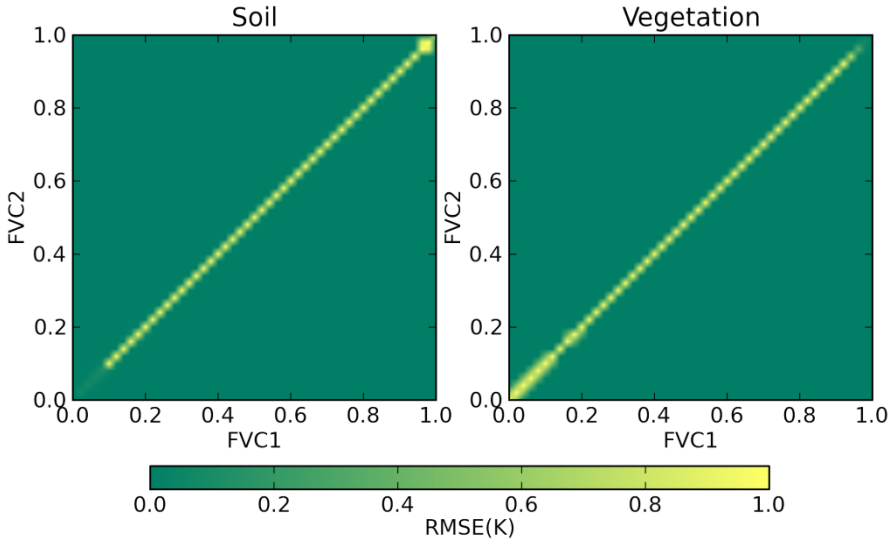


As shown in Figure 5, for most cases, the RMSEs of the estimated vegetation temperature and soil temperatures are very close to 0 K. However, when the FVCs of both simulated pixels are very close (the points in or near the diagonal line and the FVC difference within 0.04), the temperatures of the

two pixels in the mid-morning period will show very small or no differences and they can be regarded as one bigger pixel. Therefore, it results large error or high uncertainty in the estimation, and the RMSEs are usually up to tens of degrees. Under this condition, the similar radiometric temperature variation pattern of the two pixels induces a large uncertainty for the solution of Equation (7). It is also observed that the estimated soil temperature has higher accuracy than the estimated vegetation temperature when the FVCs of both pixels are very low because of the rich soil temperature information in the pixel temperature. In contrast, the estimated vegetation is more accurate than the estimated soil temperature at the high value FVC condition. The estimation was conducted without the consideration of the error of pixel temperature and FVC estimation, and the results of simulation data validation suggest that the proposed method is capable of accurately estimating the component temperatures when the neighboring pixel has different vegetation cover.

### *4.2. Uncertainty Analysis*

The above evaluation is based on the assumption that the pixel temperature and the FVC are error free. However, in real situations, due to the uncertainty of the pixel temperature and FVC estimation, errors inevitably occurred. Therefore, uncertainty analysis is needed to investigate the influence of the errors of the pixel temperature and FVC estimation on the retrieval accuracies of the estimated component temperatures.

The effects of the FVC uncertainty were analyzed first. Similar to the method mentioned in Section 4.1, the simulated LST images during the mid-morning period with two adjacent mixed pixels were selected, and the vegetation and soil component temperatures are the same as the vegetation and soil temperature variation characteristics as shown in Figure 4b in Section 3.2. In these images, the vegetation cover of one pixel is set to 40%, and another is set to 60%. Then, a Gaussian distributed random error was added to the FVC of the first pixel while the FVC of another pixel maintained the original value (60%). The random error is determined by its mean (M) and standard deviation (SD). To identify the impact of different errors, we change the mean value from 0 to 0.1 with the step of 0.01, and the standard deviation value varies from 0 to 0.2 with the step of 0.02. In total, there are 121 error cases. For each error case, 100 random errors were generated under the pre-set error mean and standard deviation and added to the FVC of the first pixel.

The proposed method was applied to these cases. For each error case, there are 100 groups of the derived vegetation and soil temperatures in this period, and the RMSE was calculated between the estimated component temperatures and the pre-defined component temperatures for each group. The average value of the RMSEs of these 100 groups was used to represent the accuracy of the estimation results in such error case. The results shown in Figure 6 reveal that the RMSEs of the estimated vegetation and soil temperature have similar distribution pattern with the change of the random error. With the increasing of the mean and standard deviation of the random error, the estimation errors of soil and vegetation temperature have an obvious increased trend. The maximum value of RMSE is more than 15 K for some cases. The accuracy of the pixel's FVC directly determines the final accuracy of the estimated soil and vegetation temperature. The relationship shows that the estimation accuracy exhibits a pretty high sensitivity to the FVC error, and the accuracy of the proposed method is highly dependent on the accuracy of the mixed pixel FVC estimation.

**Figure 6.** RMSEs of soil and vegetation temperature estimation for different fraction of vegetation cover (FVC) error cases. M: mean of FVC random error. SD: standard deviation of FVC random error.

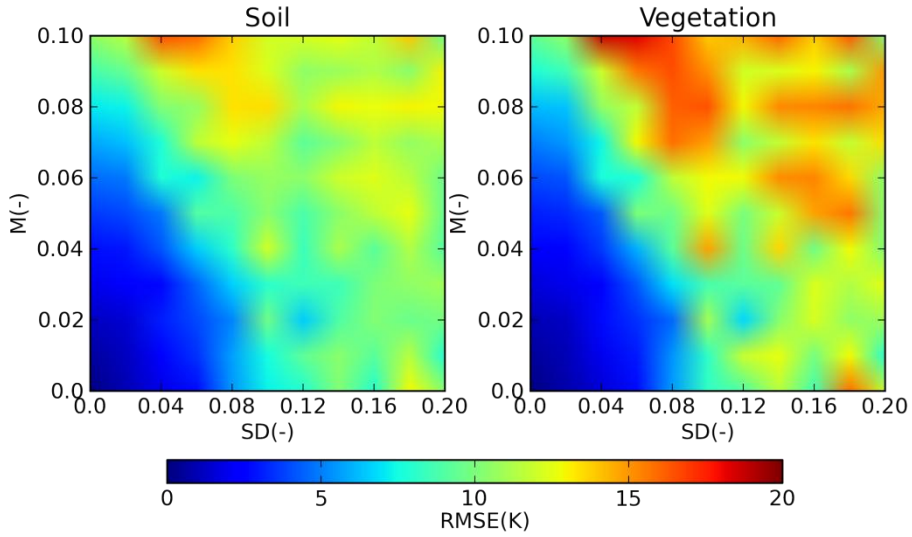


In addition to the impact of the FVC error, the influence of the uncertainty of the pixel temperature estimation should be analyzed as well. As the FVC uncertainty impact analysis, a Gaussian distributed random error was added to the pixel temperatures of the two pixels in the period. The FVCs of the two pixels are error free. The mean and the standard deviation of the random error both increase with the step of 0.04 from 0 to 4 K. Like the uncertainty analysis of the FVC error above, there are 121 pixel temperature error cases. For each error case, 100 random errors were generated and added to the temperatures of the two pixels in the mid-morning period. 100 groups of vegetation and soil component temperatures were estimated in each case and RMSE was calculated for each group. The average value of the RMSEs of these 100 groups was used to represent the accuracy of the estimation results in this error case. The RMSEs of vegetation and soil temperature estimation are presented in Figure 7. Compared with the high sensitivity to the FVC error, the method is less sensitive to the error of the pixel temperature estimation. The RMSEs do not display a significant rise when the mean and standard deviation of the temperature error increase. For these 121 error cases, most of the RMSE values are below 4K. Although the absolute value of pixel temperature is greatly influenced by the estimation uncertainties, the temporal change of pixel temperature is less affected by the uncertainties. Therefore, the temporal information used in the proposed method partly prevents the propagation of pixel estimation error to component temperature.

For the proposed algorithm, it is on the premise of linear rising process approximation of soil and vegetation temperature in the mid-morning period under clear sky condition. Generally, the linear rising process of pixel LST has been widely approved, but the rising processes of soil and vegetation temperature are less discussed. In Figure 4b, two pixels with very high and low vegetation cover condition regarded as bare soil and vegetation are picked out as an example and their LST rising process are very close to linear process with the R-squareds of 0.958 and 0.979, respectively. To further analyze the process, we focus on the linear fitting performance of low vegetation cover part (FVC $\leq$ 30%) and high vegetation cover part (FVC $\geq$ 70%), and these two parts can be approximated

to soil and vegetation surfaces. The average fitting results of these two part pixels of each in the study area are shown in Figure 8. Due to cloud cover, the R-squared and RMSE are zeros for some days. Except for these days, although the R-squareds of low FVC part are a little higher than those of high FVC part for some days, it is clear that the R-squareds keep to very high value (more than 0.8) for both parts and the RMSEs are within 1 K. Therefore, although other factors may partly influence the LST estimation results, the good regression results suggest that the temperature rising processes of soil and vegetation component obey the linear process in the mid-morning period under clear sky condition.

**Figure 7.** RMSEs of soil and vegetation temperature estimation for different pixel temperature error cases. M: mean of pixel temperature random error. SD: standard deviation of pixel temperature random error.

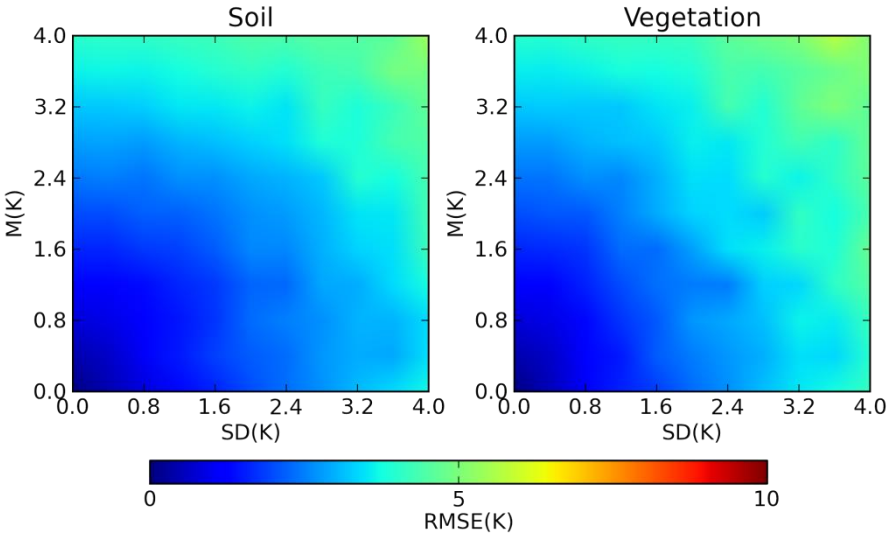


**Figure 8.** Linear regression performance of mid-morning land surface temperatures for land surface with fraction of vegetation cover (FVC) ≤ 30% and FVC ≥ 70%: (**a**) R-squared; (**b**) RMSE.

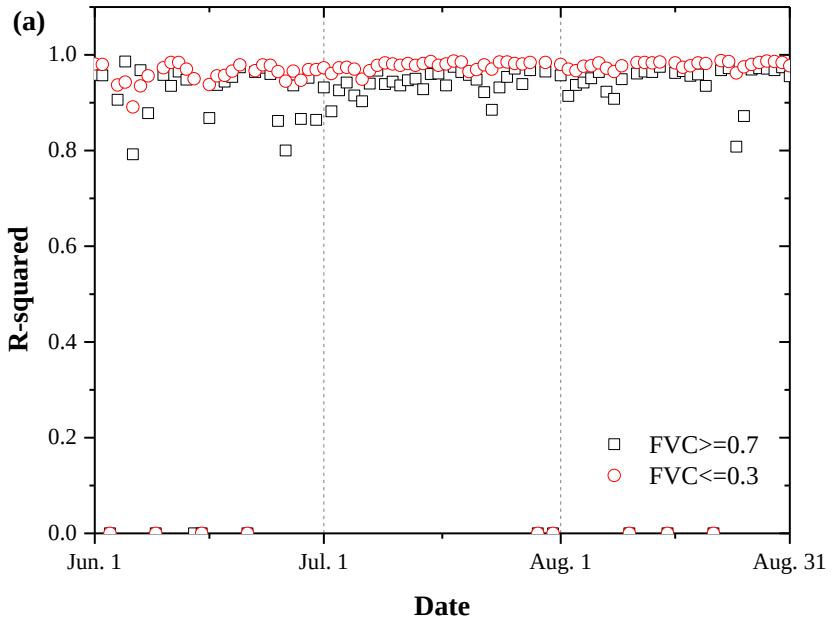

**Figure 8.** *Cont.*

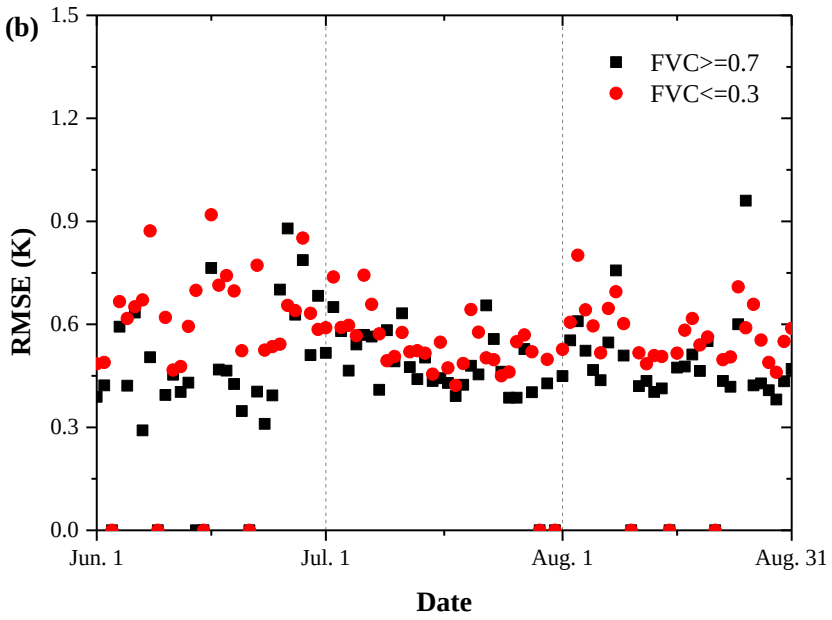


*4.3. Application to Satellite Data*

Except for the application to simulation data, the proposed method was also applied to MSG-SEVIRI products with MODIS products in the Iberian Peninsula. As neighboring pixels will be selected in the estimation, an appropriate size of the moving window should be set up in advance. The closest pixels were firstly chosen. The running results with the simulation data in Figure 5 indicate that when the FVC difference between the adjacent pixels is no more than 0.04, there will be big uncertainties in the estimation results of soil and vegetation temperatures. Therefore, we assumed that if the maximum FVC difference between the adjacent pixels and the center one is smaller than 0.05, the window size should be enlarged to make sure the 0.05 difference. Commonly, the 5 × 5 moving window is enough to satisfy this rule. As the method is under the assumption that the pixels in the moving window have the same soil and vegetation temperature at the same time, the window size should be not too large and it is limited to 9 × 9. When the window size is decided, a robust regression [60] will be performed between observation time and LST for all the pixels in the window. Ideally, as indicated before, the mid-morning temperature rising process is very close to a linear process under clear sky condition. The cloud cover condition in this period can be judged according to the LST value of each pixel at each time. When cloud cover is happened to the pixel, the LST value is set to a very low value (−80 ℃). Therefore, it is easy to detect whether the pixel in the mid-morning period based on the values in this period. However, due to some external factors, such as shortly existed thin cloud observed by satellite, cloud not detected during the observation interval and cloud shadow, the temperature variation will show small fluctuations, but the temperature rising trend will not disappear in this period. When the robust regression is conducted, the observed temperatures impacted by above factors are regarded as the outliers and they will be not involved in the regression. Finally, the pixel temperatures in this period are substituted by the fitted ones calculated from the regression coefficients, the above impacts will be partly eliminated. Figure 9 presents the flowchart in detail about the preprocessing.

**Figure 9.** Flowchart of the preprocess for the MSG-SEVIRI data.

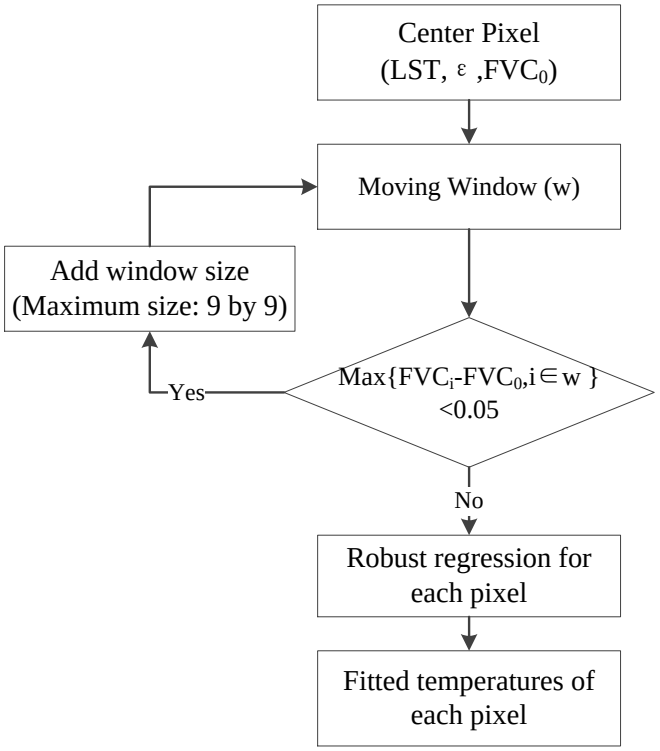


After the preprocess of MSG-SEVIRI product based on the above flowchart, soil and vegetation temperature of the study area at the TERRA satellite overpass time (about 11 a.m., local time) were derived using the TVX method with MODIS products. Due to the coarse spatial resolution of SEVIRI products compared with MODIS products, one SEVIRI pixel includes more than 10 MODIS pixels in the study area. To get the co-location information between MODIS pixels and SEVIRI pixels, the distance between each SEVIRI pixel and each MODIS pixel is calculated, based on the geo-location information of each pixel. The nearest SEVIRI pixel of one MODIS pixel is thought as the pixel containing the corresponding MODIS pixel. Generally, the soil and vegetation temperatures of the SEVIRI pixel can be calculated from the corresponding MODIS pixels. However, in some cases, there is a small NDVI variation of the MODIS pixels in one SEVIRI pixel, and it is hard to get the negative relationship between NDVI and LST. Therefore, the MODIS window should be enlarged to include more MODIS pixels in the estimation. In this study, based on the regression test with different minimum values of the NDVI range, we find that the minimum NDVI range is appropriate to be set to 0.3 and the size of the MODIS window is finally determined by the NDVI difference. Figure 10 is the estimated soil and vegetation temperatures from MODIS products at SEVIRI spatial scale and their corresponding satellite observed time in 1 July 2009. It is observed that the soil temperature is systematically higher than the vegetation temperature, and it has a relatively low value in high vegetation cover places. The satellite view time presents that the spatial difference of the satellite observation time in the study area.

**Figure 10.** Estimated soil (**a**), and vegetation (**b**), temperatures from TERRA-MODIS products using the TVX method at the satellite overpass time (**c**).

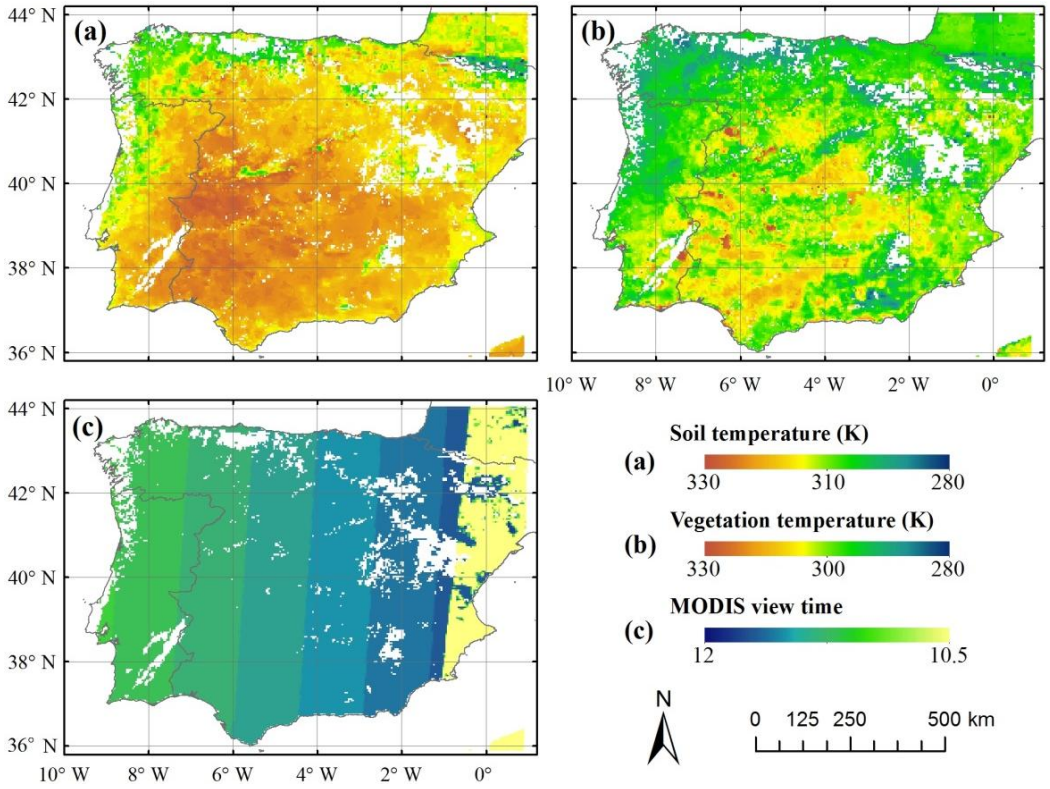


With the estimated soil and vegetation temperature using MODIS products, an additional rule was added to the component temperature estimation using SEVIRI products as introduced in Section 2. Because of the differences in instruments, algorithms and inputs in LST estimation, preview studies have indicated that the differences exist between two LST products [51,61]. In detail, the differences have been found to be time-dependent, land-cover dependent, and inversely proportional to view zenith angle differences [61]. It is difficult to eliminate the differences. Therefore, the LST differences of both products were neglected in this study. Under this assumption, the estimated component temperature should follow the constraint that the component temperature at the TERRA satellite overpass time should be no more than the estimated soil and vegetation temperature using MODIS products. Finally, the rising rates and intercepts of soil and vegetation temperatures of the study area during the mid-morning period were retrieved using the proposed method for eight cloud free days. Based on the rising rates and intercepts, the soil and vegetation temperatures of the eight days can be directly calculated. Figures 11 and 12 shows the estimated soil temperature and vegetation temperature at 9 a.m. (UTC Time) as examples. It is obvious that soil temperature is systematically higher than vegetation temperature, and the average value of soil temperature is more than 300 K. For vegetation temperature, the average value is about 290 K. From the spatial distribution pattern, it can be found that both temperatures exhibit a decrease trend from south to north, which corresponds to the distribution of the pixel temperature. The influence of vegetation cover on soil temperature is significant. In the middle and southern part of the study area, there is usually high soil temperature, while in the north, the increase of vegetation cover blocks the soil-warming process. Therefore, the temperature difference between soil and vegetation has a bigger reduction in the north. Moreover,

the vegetation temperature also has a large increase in the low vegetation cover area in the middle and southern part. The fast heating process of soil temperature accelerates the increase of vegetation temperature.

**Figure 11.** Soil temperature estimation results of the study area for eight different days at 9 a.m. (UTC), 2009.

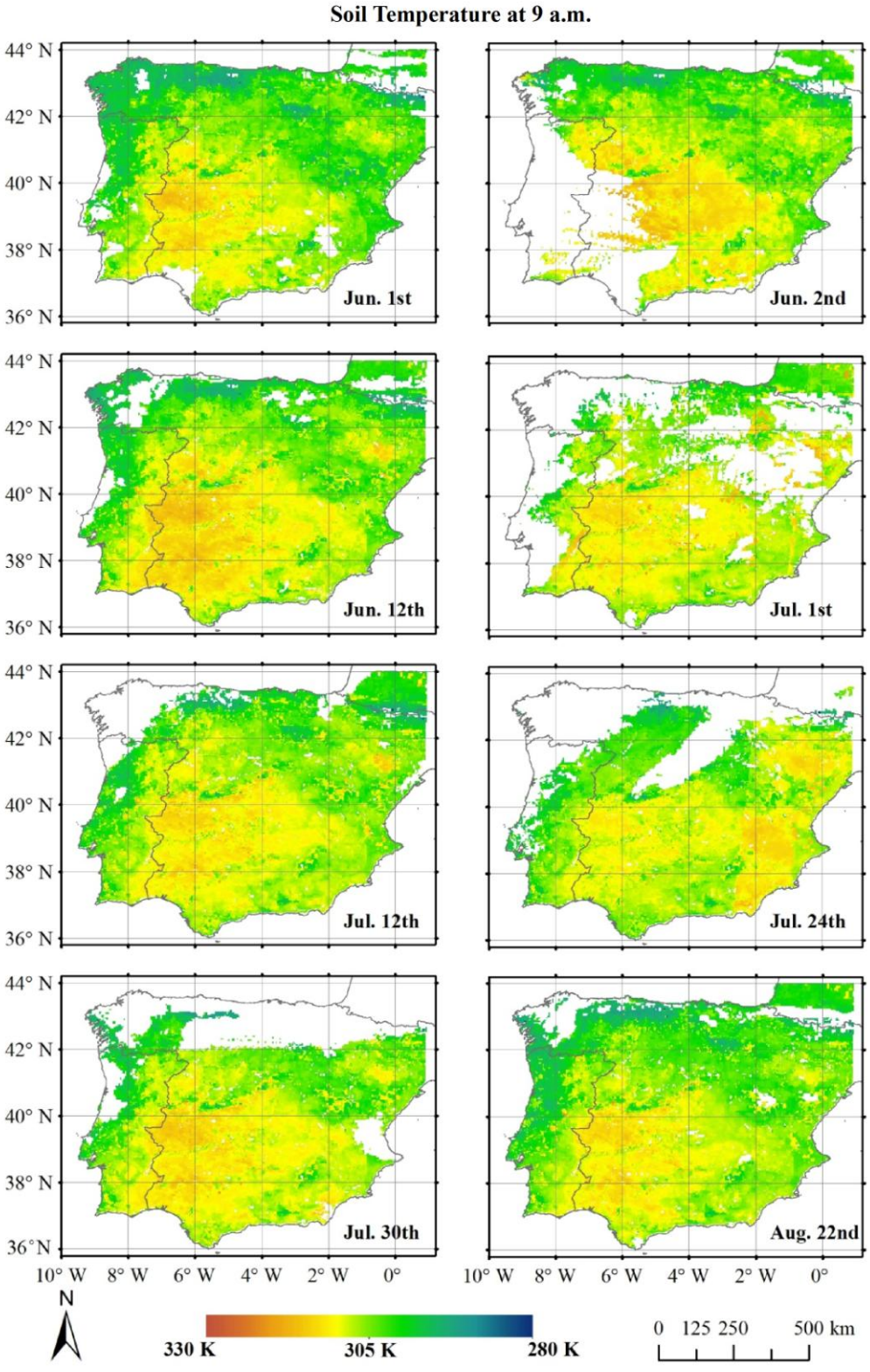

**Figure 12.** Vegetation temperature estimation results of the study area for eight different days at 9 a.m. (UTC), 2009.

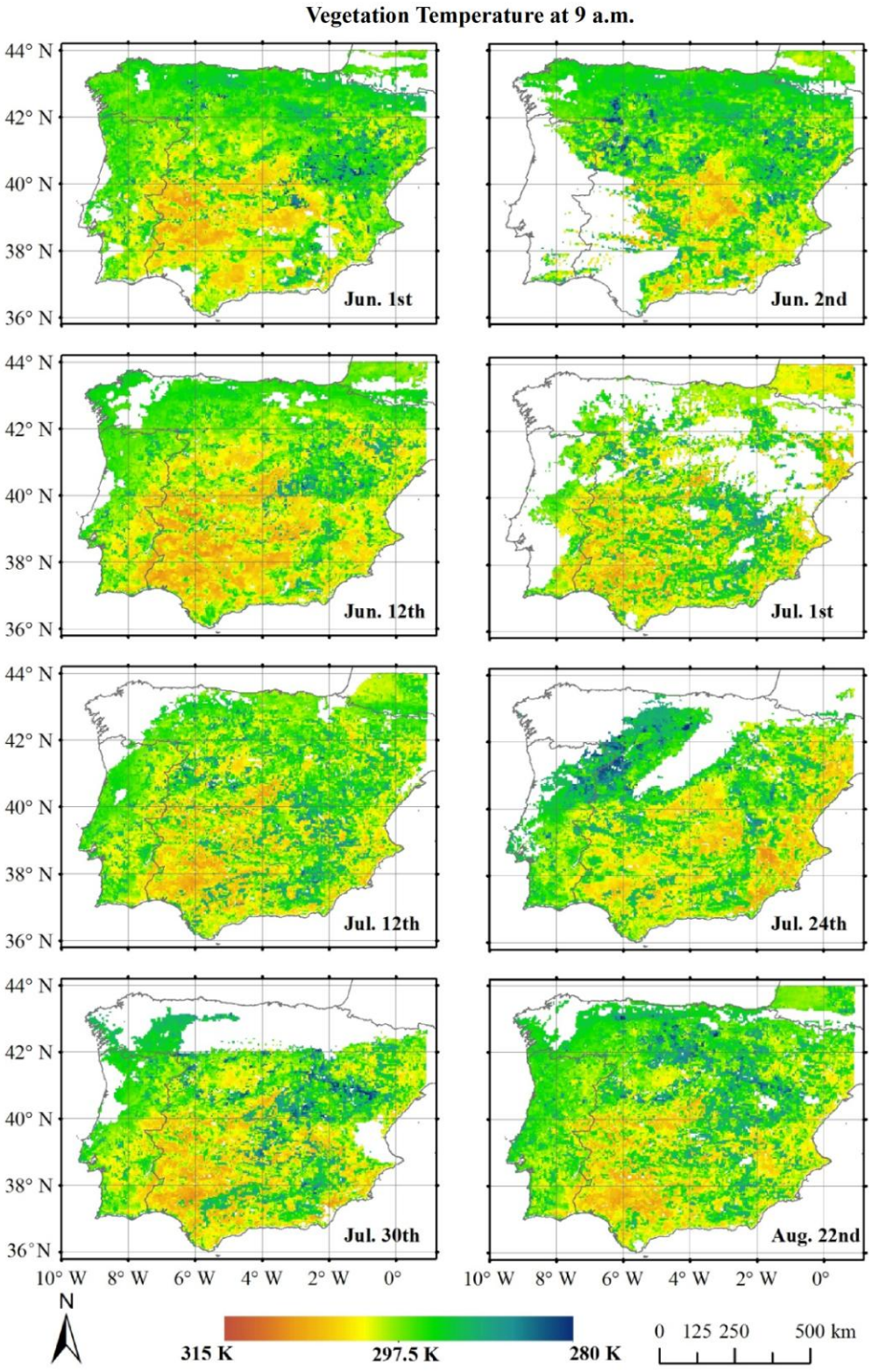


## 5. Validation and Discussion

The difficulty of obtaining *in situ* soil and vegetation temperatures at MSG SEVIRI spatial resolution is one of the major obstacles to validate the retrieved component temperatures. To partially

overcome this problem, the near surface air temperatures collected by ground atmospheric stations were compared with the estimated vegetation temperature at each site according to the canopy-air temperature equality hypothesis. Figure 13 illustrates the comparison results between the two temperatures at 9 a.m., in the eight selected days in 2009. Due to the different cloud cover conditions on different days, there are stations covered by cloud and the component temperatures are not estimated. Therefore, the comparison is conducted for these stations and the number of points shown in the subplot of Figure 13 is different from each other. In the scatter plots, the vegetation temperature has a relatively larger range than the air temperature, which can be reflected by the value of the fitting slope. The fitting slopes are all smaller than 1 for these eight days. The correlation analysis shows that there is a positive correlation between these two datasets. The R-squared changes from 0.074 to 0.423 and the RMSEs are within 4 K. The poorest correlation happened on 1 July due to a large underestimation of vegetation temperature against air temperature for some sites. In general, there are still some disagreements between two datasets and the scatter points do not exactly obey the 1:1 line. The fact can be partly explained by following reasons:

(1) The spatial representiveness difference. As mentioned above, the spatial resolution is about 5 km in the study area, thus the spatial representativeness difference between the estimated pixel vegetation temperature and the air temperature measurement at a single site will cause the inconsistence. Meanwhile, as indicated by Czajkowski *et al.* [58], the canopy-air temperature equality hypothesis is valid due to heterogeneity and shade effects at the satellite pixel scale. However, for MSG-SEVIRI pixel, these effects are not obvious especially for the pixels in the middle and southern part of the study area with extreme low vegetation cover. Under these conditions, the vegetation should have a high value and might deviate more from air temperature.

(2) The difference between air temperature and vegetation temperature. As pointed out by Jia *et al.* [38], it is not surprising to observe some differences between them in the real world. The partitioning of energy between the heat dissipation processes of a leaf, transpiration and convection, depends on environmental factors, including the radiation impinging upon a leaf and the moisture content, movement, and temperature of the air. Many environmental factors, such as radiation, convection, and transpiration, affect the vegetation temperature. The temperature difference between the leaf and the air is related to the sign and magnitude of heat exchange by convection. The dependence of stomatal conductance on temperature and moisture content of the air caused the deviation between air temperature and vegetation temperature [62].

(3) The small vegetation fraction cover. Vegetation transpiration modifies climatic conditions on the land surface during the vegetative season. Evaporative cooling caused by transpiration reduces the maximum vegetation surface temperature by about 15 ℃ on a hot and dry day [63]. However, for these atmospheric stations, more than 50% of them have low FVC values (smaller than 30%). Therefore, the heating process of the soil surface dominates the air temperature increase and the vegetation surface exerts little influence on the air temperature, which is revealed by the difference between the air temperature and vegetation temperature. The scatter plot between the air temperature and vegetation temperature of all eight days under different vegetation cover conditions are shown in Figure 14. Figure 14a includes all the sites, while Figure 14b only includes the sites whose FVCs are more than 30%. The RMSE drops greatly from 2.90 K to 2.58 K when the sites with low FVC are

excluded. The R-squared also has a big improvement from 0.231 to 0.417. In addition, the points are distributed along the 1:1 line in Figure 14b and the slope is more close to 1, which reflects the better relationship between air temperature and vegetation temperature. The result reveals that the vegetation cover cannot effectively prevent air temperature deviating greatly from vegetation temperature in the low FVC condition.

**Figure 13.** Scatter plot of the estimated vegetation temperature and *in situ* observed air temperature at 9 a.m. on the eight days in June, July and August 2009.

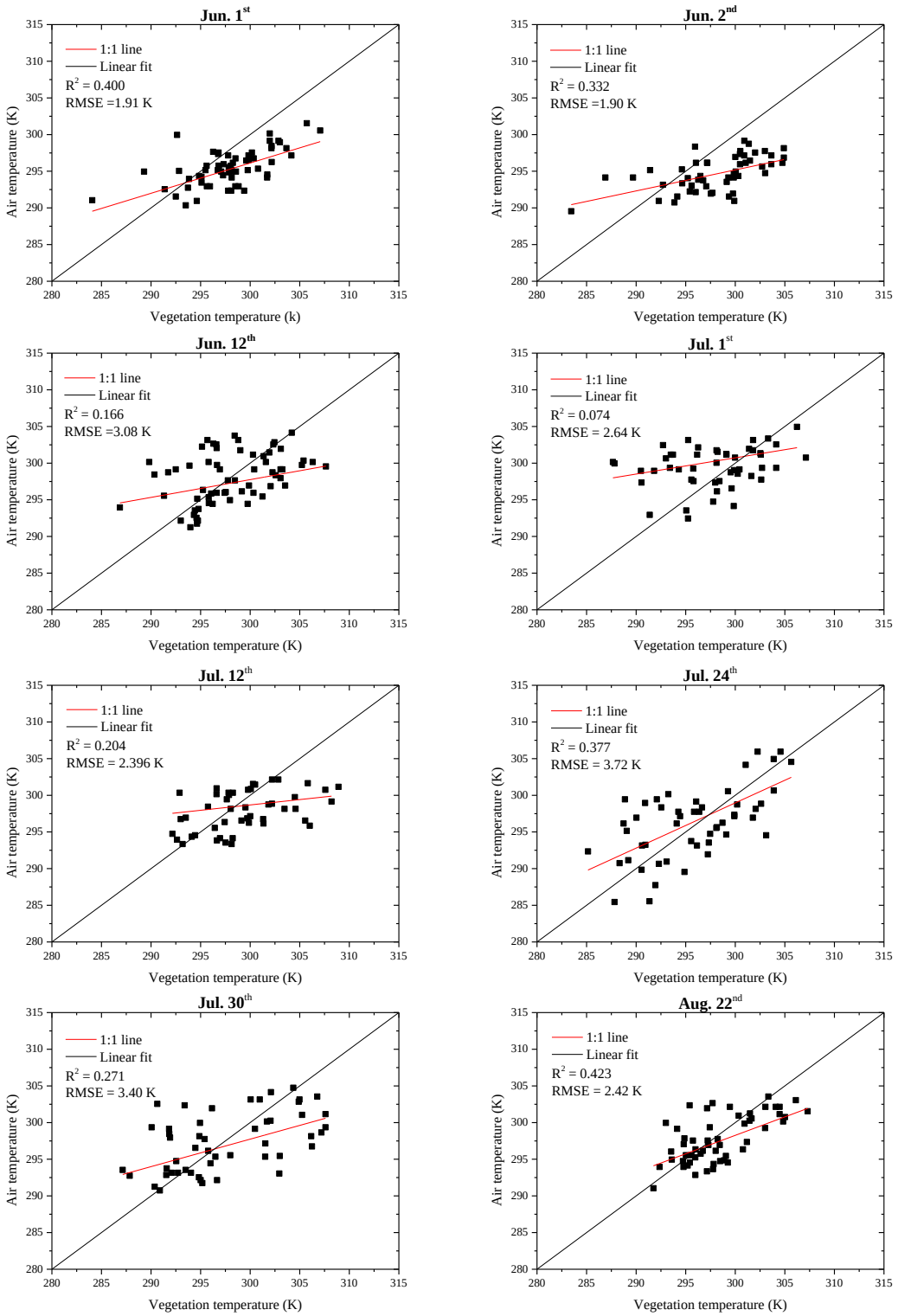

**Figure 14.** Scatter plot of the estimated vegetation temperature and site observed air temperature at 9 a.m. of the eight days, (**a**) all the sites, (**b**) the sites with FVC more than 30%.

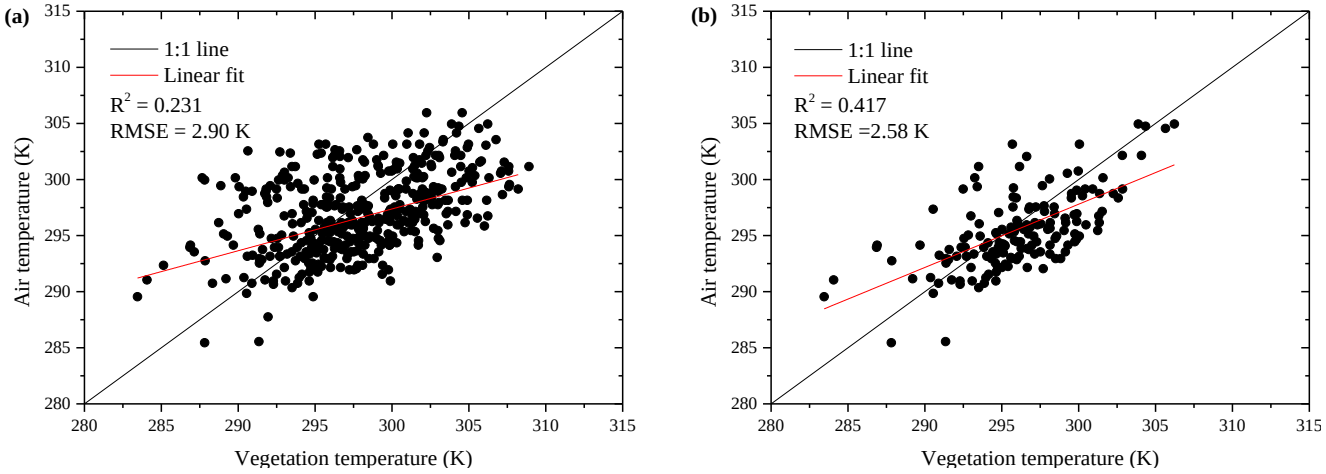


(4) The assumption of only two components. In the algorithm, we assume that land surface is only composed of soil and vegetation. In fact, it is covered with many different types of elements, especially for the big spatial pixel of SEVIRI products. Thus, the retrieved soil and vegetation temperature should be regarded as the apparent temperature, and cannot fully represent the real soil and vegetation temperature. Meanwhile, as introduced by Li *et al.* [64], an uncertainty of 1% in the emissivity in the reference channel (12 μm) can result in an error of about 0.5 K in LST. Recent research also showed the diurnal variation in surface emissivity during non-raining days [52,65,66]. Therefore, the simple setting of soil and vegetation emissivity in the study also will bring inevitable errors in soil and vegetation temperature estimation.

(5) FVC estimation error. The uncertainty analysis in Section 4.2 has proved the great impact of FVC estimation error on the soil and vegetation temperature retrieval. However, the implement of the algorithm is based on the fact that the FVC functions well, and that the FVC value controls the ratio of the soil or vegetation temperature in the whole pixel temperature information. Therefore, in the component temperature estimation process, the FVC value determines the exact value of the soil and vegetation component temperatures, and the errors in the estimation of the FVC influence the accuracy of the component temperature estimation.

(6) The LST product error. Except for the uncertainty in LST estimation for both SEVIRI and MODIS products, the cold bias is also one important error source. The assessment study of remotely sensed land surface temperature by Trigo *et al.* [51] has found that the both SEVIRI and MODIS tend to underestimate local measurements, with colder values obtained with MODIS. It agrees with the results of the study [67] that compare MODIS LST with ground measurements over land. As an important input in the method, the cold bias of MODIS LST product will influence the values of the estimated soil and vegetation temperature.

## 6. Conclusions

This study presents a practical algorithm for deriving soil and vegetation component temperatures in the mid-morning period by combining multi-spectral and time series observations from Meteosat Second Generation (MSG) Spinning Enhanced Visible and Infrared Imager (SEVIRI) and instantaneous observation from TERRA-MODIS. The synergetic use of SEVIRI and MODIS products provides a new idea for component temperature estimation by using the spatial and temporal advantages of both data. In general, this study is a preliminary research. Many assumptions have been built and many approximations are made to carry out the estimation. The derived soil and vegetation temperatures will be useful to improve surface energy balance and soil moisture estimation at regional or continental scale. However, further study is still needed by adding additional information to reduce the sensitivity of estimation results on vegetation cover accuracy. The emissivity variation and the cold bias should also been included in future work. A direct validation is also needed to fully evaluate the estimation results with *in situ* soil and vegetation temperature measurements.

## Acknowledgments

This research was jointly supported by the "Hundred Talents" Project, the Key Research Program (KZZD-EW-08-01), the International Cooperation Partner Program of Innovative Team (Grant No. KZZD-EW-TZ-06) of Chinese Academy of Sciences, National natural science foundation project (41271433), the External Cooperation Program of BIC, Chinese Academy of Sciences (GJHZ201320) and Youth foundation of IMHE, 2013.

## Author Contributions

All authors have made major and unique contributions. Ainong Li assisted the methodology development, supervised and participated with the work throughout all phases including the manuscript writing and revision. Huaan Jin and Zhengjian Zhang took part in data collection and preprocessing. Jinhu Bian performed the data validation analysis. Wei Zhao performed the data generation, data comparison analysis, results interpretation, manuscript writing, and coordinated the revision activities.

## Conflicts of Interest

The authors declare no conflict of interest.

## References

1. Wan, Z.; Zhang, Y.; Zhang, Q.; Li, Z.L. Quality assessment and validation of the MODIS global land surface temperature. *Int. J. Remote Sens.* **2004**, *25*, 261–274.
2. Bertoldi, G.; Notarnicola, C.; Leitinger, G.; Endrizzi, S.; Zebisch, M.; Della Chiesa, S.; Tappeiner, U. Topographical and ecohydrological controls on land surface temperature in an alpine catchment. *Ecohydrology* **2010**, *3*, 189–204.

3. Claps, P.; Laguardia, G. Assessing spatial variability of soil water content through thermal inertia and NDVI. *Proc. SPIE* **2004**, *5232*, 378–387.
4. Tomlinson, C.J.; Chapman, L.; Thornes, J.E.; Baker, C. Remote sensing land surface temperature for meteorology and climatology: A review. *Meteorol. Appl.* **2011**, *18*, 296–306.
5. Li, Z.-L.; Tang, R.; Wan, Z.; Bi, Y.; Zhou, C.; Tang, B.; Yan, G.; Zhang, X. A review of current methodologies for regional evapotranspiration estimation from remotely sensed data. *Sensors* **2009**, *9*, 3801–3853.
6. Li, Z.-L.; Tang, B.-H.; Wu, H.; Ren, H.; Yan, G.; Wan, Z.; Trigo, I.F.; Sobrino, J.A. Satellite-derived land surface temperature: Current status and perspectives. *Remote Sens. Environ.* **2013**, *131*, 14–37.
7. Becker, F.; Li, Z.-L. Towards a local split window method over land surfaces. *Int. J. Remote Sens.* **1990**, *11*, 369–393.
8. Jiang, G.-M.; Li, Z.-L.; Nerry, F. Land surface emissivity retrieval from combined mid-infrared and thermal infrared data of MSG-SEVIRI. *Remote Sens. Environ.* **2006**, *105*, 326–340.
9. Li, Z.-L.; Becker, F. Feasibility of land surface temperature and emissivity determination from AVHRR data. *Remote Sens. Environ.* **1993**, *43*, 67–85.
10. Sobrino, J.A.; Romaguera, M. Land surface temperature retrieval from MSG1-SEVIRI data. *Remote Sens. Environ.* **2004**, *92*, 247–254.
11. Sun, D.; Pinker, R.T. Retrieval of surface temperature from the MSG-SEVIRI observations: Part I. Methodology. *Int. J. Remote Sens.* **2007**, *28*, 5255–5272.
12. Tang, B.; Bi, Y.; Li, Z.-L.; Xia, J. Generalized split-window algorithm for estimate of land surface temperature from Chinese geostationary FengYun meteorological satellite (FY-2C) data. *Sensors* **2008**, *8*, 933–951.
13. Cho, A.-R.; Suh, M.-S. Evaluation of land surface temperature operationally retrieved from Korean geostationary satellite (COMS) Data. *Remote Sens.* **2013**, *5*, 3951–3970.
14. Anderson, M.C.; Allen, R.G.; Morse, A.; Kustas, W.P. Use of landsat thermal imagery in monitoring evapotranspiration and managing water resources. *Remote Sens. Environ.* **2012**, *122*, 50–65.
15. Stisen, S.; Sandholt, I.; Nørgaard, A.; Fensholt, R.; Eklundh, L. Estimation of diurnal air temperature using MSG SEVIRI data in West Africa. *Remote Sens. Environ.* **2007**, *110*, 262–274.
16. Tang, R.; Li, Z.-L.; Tang, B. An application of the Ts–VI triangle method with enhanced edges determination for evapotranspiration estimation from MODIS data in arid and semi-arid regions: Implementation and validation. *Remote Sens. Environ.* **2010**, *114*, 540–551.
17. Zhao, W.; Li, Z.-L. Sensitivity study of soil moisture on the temporal evolution of surface temperature over bare surfaces. *Int. J. Remote Sens.* **2013**, *34*, 3314–3331.
18. Meng, F.; Liu, M. Remote-sensing image-based analysis of the patterns of urban heat islands in rapidly urbanizing Jinan, China. *Int. J. Remote Sens.* **2013**, *34*, 8838–8853.
19. Ogashawara, I.; Bastos, V. A Quantitative approach for analyzing the relationship between urban heat islands and land cover. *Remote Sens.* **2012**, *4*, 3596–3618.
20. Zakšek, K.; Oštir, K. Downscaling land surface temperature for urban heat island diurnal cycle analysis. *Remote Sens. Environ.* **2012**, *117*, 114–124.

21. Gao, F.; Kustas, W.; Anderson, M. A data mining approach for sharpening thermal satellite imagery over land. *Remote Sens.* **2012**, *4*, 3287–3319.
22. Bechtel, B.; Zakšek, K.; Hoshyaripour, G. Downscaling land surface temperature in an urban area: A case study for Hamburg, Germany. *Remote Sens.* **2012**, *4*, 3184–3200.
23. Song, X.; Zhao, Y. Study on component temperatures inversion using satellite remotely sensed data. *Int. J. Remote Sens.* **2007**, *28*, 2567–2579.
24. Shi, Y. Thermal infrared inverse model for component temperatures of mixed pixels. *Int. J. Remote Sens.* **2011**, *32*, 2297–2309.
25. Geiger, R.; Aron, R.H.; Todhunter, P. *Climate near the Ground*, 6th ed.; Rowman & Littlefield: Lanham, MD, USA, 2003.
26. Li, Z.-L.; Wu, H.; Wang, N.; Qiu, S.; Sobrino, J.A.; Wan, Z.; Tang, B.-H.; Yan, G. Land surface emissivity retrieval from satellite data. *Int. J. Remote Sens.* **2013**, *34*, 3084–3127.
27. Li, Z.-L.; Stoll, M.P.; Zhang, R.H.; Jia, L.; Su, Z. On the separate retrieval of soil and vegetation temperatures from ATSR data. *Sci. China Ser. D* **2001**, *44*, 97–111.
28. Liu, D.; Pu, R. Downscaling thermal infrared radiance for subpixel land surface temperature retrieval. *Sensors* **2008**, *8*, 2695–2706.
29. Yang, G.; Pu, R.; Zhao, C.; Huang, W.; Wang, J. Estimation of subpixel land surface temperature using an endmember index based technique: A case examination on ASTER and MODIS temperature products over a heterogeneous area. *Remote Sens. Environ.* **2011**, *115*, 1202–1219.
30. Dozier, J. A method for satellite identification of surface temperature fields of subpixel resolution. *Remote Sens. Environ.* **1981**, *11*, 221–229.
31. Rasmussen, M.O.; Goettsche, F.-M.; Olesen, F.-S.; Sandholt, I. Directional effects on land surface temperature estimation from meteosat second generation for Savanna landscapes. *IEEE Trans. Geosci. Remote Sens.* **2011**, *49*, 4458–4468.
32. Cuenca, J.; Sobrino, J.A. Experimental measurements for studying angular and Spectral variation of thermal infrared emissivity. *Appl. Opt.* **2004**, *43*, 4598–4602.
33. Kimes, D.S. Remote sensing of row crop structure and component temperatures using directional radiometric temperatures and inversion techniques. *Remote Sens. Environ.* **1983**, *13*, 33–55.
34. Rees, W.G.; James, S.P. Angular variation of the infrared emissivity of ice and water surfaces. *Int. J. Remote Sens.* **1992**, *13*, 2873–2886.
35. Sobrino, J.; Caselles, V. Thermal infrared radiance model for interpreting the directional radiometric temperature of a vegetative surface. *Remote Sens. Environ.* **1990**, *33*, 193–199.
36. Li, Z.-L.; Zhang, R.; Sun, X.; Su, H.; Tang, X.; Zhu, Z.; Sobrino, J. Experimental system for the study of the directional thermal emission of natural surfaces. *Int. J. Remote Sens.* **2004**, *25*, 195–204.
37. Wang, J.; Li, X.; Sun, X.; Liu, Q. Component temperatures inversion for remote sensing pixel based on directional thermal radiation model. *Sci. China Ser. E* **2000**, *43*, 41–47.
38. Jia, L.; Li, Z.-L.; Menenti, M.; Su, Z.; Verhoef, W.; Wan, Z. A practical algorithm to infer soil and foliage component temperatures from bi-angular ATSR-2 data. *Int. J. Remote Sens.* **2003**, *24*, 4739–4760.

39. Menenti, M.; Jia, L.; Li, Z.-L.; Djepa, V.; Wang, J.; Stoll, M.P.; Su, Z.; Rast, M. Estimation of soil and vegetation temperatures with multiangular thermal infrared observations: IMGRASS, HEIFE, and SGP 1997 experiments. *J. Geophys. Res.: Atmos.* **2001**, *106*, 11997–12010.
40. Norman, J.M.; Kustas, W.P.; Humes, K.S. Source approach for estimating soil and vegetation energy fluxes in observations of directional radiometric surface temperature. *Agric. For. Meteorol.* **1995**, *77*, 263–293.
41. Becker, F.; Li, Z.-L. Temperature-independent spectral indices in thermal infrared bands. *Remote Sens. Environ.* **1990**, *32*, 17–33.
42. Wetzel, P.J.; Atlas, D.; Woodward, R.H. Determining soil moisture from geosynchronous satellite infrared data: A feasibility study. *J. Appl. Meteorol.* **1984**, *23*, 375–391.
43. Zhao, W.; Li, A. A Downscaling method for improving the spatial resolution of AMSR-E derived soil moisture product based on MSG-SEVIRI data. *Remote Sens.* **2013**, *5*, 6790–6811.
44. Goward, S.N.; Xue, Y.; Czajkowski, K.P. Evaluating land surface moisture conditions from the remotely sensed temperature/vegetation index measurements: An exploration with the simplified simple biosphere model. *Remote Sens. Environ.* **2002**, *79*, 225–242.
45. Prihodko, L.; Goward, S.N. Estimation of air temperature from remotely sensed surface observations. *Remote Sens. Environ.* **1997**, *60*, 335–346.
46. Peres, L.F.; DaCamara, C.C. Land surface temperature and emissivity estimation based on the two-temperature method: Sensitivity analysis using simulated MSG/SEVIRI data. *Remote Sens. Environ.* **2004**, *91*, 377–389.
47. Stisen, S.; Sandholt, I.; Nørgaard, A.; Fensholt, R.; Jensen, K.H. Combining the triangle method with thermal inertia to estimate regional evapotranspiration—Applied to MSG-SEVIRI data in the Senegal River basin. *Remote Sens. Environ.* **2008**, *112*, 1242–1255.
48. Bennouna, Y.S.; Curier, L.; de Leeuw, G.; Piazzola, J.; Roebeling, R.; de Valk, P. An automated day-time cloud detection technique applied to MSG-SEVIRI data over Western Europe. *Int. J. Remote Sens.* **2010**, *31*, 6073–6093.
49. Sobrino, J.A.; Jiménez-Muñoz, J.C.; El-Kharraz, J.; Gómez, M.; Romaguera, M.; Sòria, G. Single-channel and two-channel methods for land surface temperature retrieval from DAIS data and its application to the Barrax site. *Int. J. Remote Sens.* **2004**, *25*, 215–230.
50. Jiang, G.M.; Li, Z.L. Split-window algorithm for land surface temperature estimation from MSG1-SEVIRI data. *Int. J. Remote Sens.* **2008**, *29*, 6067–6074.
51. Trigo, I.F.; Monteiro, I.T.; Olesen, F.; Kabsch, E. An assessment of remotely sensed land surface temperature. *J. Geophys. Res.: Atmos.* **2008**, *113*, doi:10.1029/2008JD010035.
52. Masiello, G.; Serio, C.; de Feis, I.; Amoroso, M.; Venafra, S.; Trigo, I.; Watts, P. Kalman filter physical retrieval of surface emissivity and temperature from geostationary infrared radiances. *Atmos. Meas. Tech.* **2013**, *6*, 3613–3634.
53. Land surface analysis satellite applications facility. Available online: https://landsaf.meteo.pt/ (accessed on 1 December 2013).
54. Wan, Z.M.; Dozier, J. A generalized split-window algorithm for retrieving land-surface temperature from space. *IEEE Trans. Geosci. Remote Sens.* **1996**, *34*, 892–905.
55. Garcia-Haro, F.J.; Sommer, S.; Kemper, T. A new tool for variable multiple endmember spectral mixture analysis (VMESMA). *Int. J. Remote Sens.* **2005**, *26*, 2135–2162.

56. Reverb. Available online: http://reverb.echo.nasa.gov/reverb (accessed on 1 December 2013).
57. Ehrler, W.L. Cotton leaf temperatures as related to soil-water depletion and meteorological factors *Agron. J.* **1973**, *65*, 404–409.
58. Czajkowski, K.P.; Mulhern, T.; Goward, S.N.; Cihlar, J.; Dubayah, R.O.; Prince, S.D. Biospheric environmental monitoring at BOREAS with AVHRR observations. *J. Geophys. Res.: Atmos.* **1997**, *102*, 29651–29662.
59. NCDC Climate Data Online. Available online: http://www.ncdc.noaa.gov/cdo-web/ (accessed on 1 December 2013).
60. Rousseeuw, P.J.; Leroy, A.M. *Robust Regression and Outlier Detection*; Wiley: Hoboken, NJ, USA, 2005; Volume 589.
61. Gao, C.; Jiang, X.; Wu, H.; Tang, B.; Li, Z.; Li, Z.-L. Comparison of land surface temperatures from MSG-2/SEVIRI and Terra/MODIS. *J. Appl. Remote Sens.* **2012**, *6*, doi:10.1117/1.JRS.6.063606.
62. Drake, B.G.; Raschke, K.; Salisbury, F.B. Temperature and transpiration resistances of Xanthium leaves as affected by air temperature, humidity, and wind speed. *Plant Physiol.* **1970**, *46*, 324–330.
63. Novak, V.; Havrila, J. Method to estimate the critical soil water content of limited availability for plants. *Biologia* **2006**, *61*, S289–S293.
64. Li, Z.-L.; Becker, F.; Stoll, M.; Wan, Z. Evaluation of six methods for extracting relative emissivity spectra from thermal infrared images. *Remote Sens. Environ.* **1999**, *69*, 197–214.
65. Li, Z.; Li, J.; Li, Y.; Zhang, Y.; Schmit, T.J.; Zhou, L.; Goldberg, M.D.; Menzel, W.P. Determining diurnal variations of land surface emissivity from geostationary satellites. *J. Geophys. Res.: Atmos.* **2012**, *117*, doi:10.1029/2012JD018279.
66. Masiello, G.; Serio, C.; Venafra, S.; DeFeis, I.; Borbas, E.E. Diurnal variation in Sahara desert sand emissivity during the dry season from IASI observations. *J. Geophys. Res.: Atmos.* **2014**, doi:10.1002/jgrd.50863.
67. Bosilovich, M.G. A comparison of MODIS land surface temperature with *in situ* observations. *Geophys. Res. Lett.* **2006**, *33*, doi:10.1029/2006GL027519.